Evaluation of the influence of voids on 3D representative volume elements of fiber-reinforced polymer composites using CUF micromechanics

Evaluation of the influence of voids on 3D representative volume elements of fiber-reinforced polymer composites using CUF micromechanics

E. Carrera[*], M. Petrolo[†], M.H. Nagaraj[‡], M. Delicata[§]

MUL^2 Group, Department of Mechanical and Aerospace Engineering, Politecnico di Torino
Turin, Italy

Revised version of COMSTR-D-20-00032

Author for correspondence:
Marco Petrolo
MUL^2 Group, Department of Mechanical and Aerospace Engineering,
Politecnico di Torino,
Corso Duca degli Abruzzi 24,
10129 Torino, Italy,
tel: +39 011 090 6845,
fax: +39 011 090 6899,
e-mail: marco.petrolo@polito.it

[*]Professor of Aerospace Structures and Aeroelasticity, erasmo.carrera@polito.it
[†]Associate Professor, marco.petrolo@polito.it
[‡]Ph.D. Student, manish.nagaraj@polito.it
[§]Research Assistant, michele.delicata@polito.it

Abstract

This paper presents numerical results on the micromechanics linear analysis of representative volume elements (RVE) containing voids. The modeling approach is the micromechanical framework within the Carrera Unified Formulation in which fibers and matrix are 1D finite elements (FE) with enriched kinematics and component-wise capabilities. RVE models are 3D and consider all six stress components. Such a modeling strategy leads to a twofold reduction of the degrees of freedom as compared to 3D FE. The numerical assessments address the influence of the volume fraction and distribution of voids, including comparisons with data from the literature and statistical studies regarding homogenized properties and stress fields. The proposed modeling approach can capture the local effects due to the presence of voids, and, given its computational efficiency, the present framework is promising for nonlinear analysis, such as progressive failure.

Keywords: Voids, micromechanics, CUF, fiber reinforced polymers

1 Introduction

Fiber-reinforced composites are increasingly popular in many engineering fields to provide superior performances as compared to metals [1, 2]. In addition to space and aeronautics industries, the automotive and energy sector are making growing use of these materials due to the lightweight and the high specific strength and stiffness [3, 4]. Composites have a multiscale nature, and the proper prediction of fundamental mechanical behavior requires modeling of the various scales. The present paper focuses on the microscale in which the differences between constituent properties and the presence of interfaces and defects lead to modeling challenges [5]. Defects stemming from manufacturing can significantly modify the microscale characteristics and lead to various damage mechanisms, such as [2, 6] interfacial debonding and sliding, matrix microcracking, delamination, fiber breakage, and fiber micro-buckling.

The present paper deals with the numerical modeling of voids in the matrix. Voids can influence the matrix-dominated mechanical properties and lead to the localization of stresses [7]. Many works have investigated the void formation, growth, morphology, and influence on structural performance. The work of Mehdikhani et al. [8] is a comprehensive guide for the selection of these studies.

Computational micromechanics is a popular tool to study defects and related issues. By the direct modeling of the microscale components and defects, micromechanics can provide the homogenized macroscopic mechanical properties and, via de-homogenization, the stress and strain fields at the microscale. Various numerical approaches, e.g., finite elements (FE), can model the microscale via the use of a representative volume element (RVE) containing the typical architecture of the composite structure in hand [9–18]. Other works investigate the effect of voids in the elastic regime and strength prediction, embedding them into the FE model and considering various loading conditions and failure modes [3, 5, 19–30].

The use of FE models can lead to very high computational costs. Such costs may be prohibitive when the 3D structure of the RVE is of interest, or nonlinear analyses are necessary. The present work falls within the Carrera Unified Formulation (CUF) use for micromechanics [31–33]. One of the advantages of CUF is the possibility of modeling multi-component structures as an ensemble of 1D finite elements with enriched cross-section kinematics [34]. Such a capability significantly reduces the computational costs - as there are no aspect ratio constraints - but retains 3D-like accuracy for all stress and strain components. Functions adopted to model the structural behavior are independent of the shape functions. For instance, in a 2D case, Lagrange or Legendre polynomials can be used as shape functions, and Mac-Laurin or harmonics

can be used over the thickness. The latter defines the structural theory adopted with classical ones – CLT and FSDT – as special cases. Similarly, in a 1D case, in which the shape functions act along one direction and the expansion functions over the other two. Such a separation allows one to avoid the aspect ratio constraints over one or more directions and retain the accuracy of 3D models by enriching the structural theory, i.e., the expansion functions. In other words, the accuracy of the model is augmented via richer theories rather than more refined discretizations. CUF for linear and nonlinear multiscale problems provided twofold reductions on computational costs as compared to 3D FE [35, 36].

The objective of the present work is to investigate the influence of microscale matrix voids on the macroscopic mechanical properties and the microscopic fields. For the first time, CUF is used to model 3D RVE and voids. The modeling of voids includes their volume fraction and distribution. This paper is organized as follows: Sections 2 and 3 describe the theoretical framework for FE and micromechanics, respectively. The numerical results are in Section 4, and conclusions in Section 5.

2 Higher-order 1D structural theories

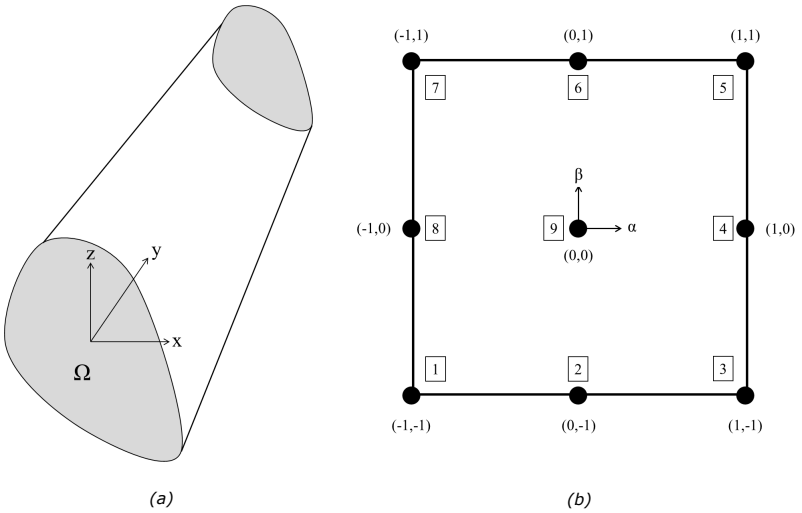

Figure 1: (a) Beam with arbitrary cross-section oriented along the y-axis, and (b) the 9-node bi-quadratic Lagrange expansion element in the natural coordinate system

Considering a beam oriented along the y-axis, as shown in Fig. 1(a), the displacement field in CUF is

$$\mathbf{u} = F_\tau(x,z)\mathbf{u}_\tau(y), \tau = 1,2,\dots M \tag{1}$$

Where $\mathbf{u}$ is the displacement field and $F_\tau(x,z)$ is the expansion function across the cross-section. $\mathbf{u}_\tau$ is the generalized displacement vector, and M is the number of terms in the expansion function. The choice of F_τ and M is arbitrary. The present work utilizes the Lagrange Expansion (LE) class of expansions to enhance the cross-section kinematics, resulting in a Component-Wise (CW) model. In this approach, Lagrange polynomials explicitly discretize the cross-section geometry and displacement field. This work uses 9-node bi-quadratic expansion elements (L9), see Fig. 1(b), in which the 3D displacement field is

$$\begin{aligned} u_x &= \sum_{\tau=1}^{9} F_\tau(x,z) \cdot u_{x_\tau}(y) \\ u_y &= \sum_{\tau=1}^{9} F_\tau(x,z) \cdot u_{y_\tau}(y) \\ u_z &= \sum_{\tau=1}^{9} F_\tau(x,z) \cdot u_{z_\tau}(y) \end{aligned} \tag{2}$$

The use of Lagrange expansion results in a 1D numerical model that explicitly models the 3D domain without the need of fictitious entities like the reference axis. The CUF formulation adopted in this paper is 1D, as the unknown variables depend on the y-direction. In other words, the shape functions are functions of y. Over the other two directions, x and z, the structural theory modeling acts via the expansion functions. Given a node along the y-axis, a set of unknowns is defined by the expansion functions. In the classical 1D models, e.g., Timoshenko, each node has five unknowns. In CUF, the number of nodal unknowns, or degrees of freedom, can be changed freely depending on the structural theory adopted. In the 1D case, a beam-axis has to be defined over the 3D body, and the unknowns are placed over that axis. In the 2D case, a reference plane is defined for the same purpose. Such a task may be difficult and lead to inaccurate modeling of the geometry, and weaker accuracy as the distance from the axis grows. In the CUF formulation adopted in this paper, the use of Lagrange polynomials over the cross-section allows one to model the geometry more accurately as the unknown variables can be placed uniformly over the area and even over the edges. Furthermore, the displacement field consists of only translational degrees of freedom (DOF), without involving rotations. Further details on the use of Lagrange polynomials as expansion functions can be found in [37].

The stress and strain fields in vector notation are

$$\begin{aligned} \boldsymbol{\sigma} &= \{\sigma_{xx}, \sigma_{yy}, \sigma_{zz}, \sigma_{xy}, \sigma_{xz}, \sigma_{yz}\}^T \\ \boldsymbol{\epsilon} &= \{\epsilon_{xx}, \epsilon_{yy}, \epsilon_{zz}, \epsilon_{xy}, \epsilon_{xz}, \epsilon_{yz}\}^T \end{aligned} \tag{3}$$

Assuming linear strains, the displacements are related to the strains as

$$\boldsymbol{\epsilon} = \mathbf{D} \cdot \mathbf{u} \tag{4}$$

where $\mathbf{D}$ is the linear differentiation operator given by

$$\mathbf{D} = \begin{bmatrix} \frac{\partial}{\partial x} & 0 & 0 \\ 0 & \frac{\partial}{\partial y} & 0 \\ 0 & 0 & \frac{\partial}{\partial z} \\ \frac{\partial}{\partial y} & \frac{\partial}{\partial x} & 0 \\ \frac{\partial}{\partial z} & 0 & \frac{\partial}{\partial x} \\ 0 & \frac{\partial}{\partial z} & \frac{\partial}{\partial y} \end{bmatrix}$$

The constitutive law, considering an elastic material behavior, is

$$\boldsymbol{\sigma} = \mathbf{C}\boldsymbol{\epsilon} \tag{5}$$

where $\mathbf{C}$ is the linear elastic material matrix. The structure is discretized in the axial direction using beam elements, interpolated using the nodal shape functions N_i. In this work, four-node beam elements (B4) were used. The combination of beam elements and cross-section expansions results in a 3D displacement field defined as

$$\mathbf{u}(x, y, z) = F_\tau(x, z) N_i(y) \mathbf{u}_{\tau i} \tag{6}$$

where $\mathbf{u}_{\tau i}$ is the nodal displacement field. Based on the principle of virtual displacements,

$$\delta L_{int} = \delta L_{ext} \tag{7}$$

where δL_{int} is the virtual variation of the internal strain energy,

$$\delta L_{int} = \int_V \delta \boldsymbol{\epsilon}^T \boldsymbol{\sigma} \tag{8}$$

L_{ext} is the work due to the externally applied load,

$$L_{ext} = F_s N_j \delta \mathbf{u}_{sj}^T \mathbf{P} \tag{9}$$

where $\mathbf{P}$ is the external force vector. Using Eqs. (5), (6) and (8), the stiffness matrix is defined as

$$\delta L_{int} = \delta \mathbf{u}_{sj}^T \mathbf{k}_{ij\tau s} \mathbf{u}_{\tau i} \tag{10}$$

with

$$\mathbf{k}_{ij\tau s} = \int_l \int_\Omega \mathbf{D}^T (N_i(y) F_\tau(x,z)) \mathbf{C} \mathbf{D} (N_j(y) F_s(x,z)) \; d\Omega \; dl \tag{11}$$

$\mathbf{k}_{ij\tau s}$ is the 3x3 Fundamental Nucleus (FN), and is invariant with respect to the applied structural theory. Ω and l represent the cross-section domain and beam length, respectively. The stiffness matrix changes as the structural theory do so. Changes are due not only to the different approaches, i.e., beams or plates, but also to the order of the structural theory, e.g., Euler-Bernoulli, Timoshenko, Third Order Shear Deformation. Most of the literature's approaches require ad hoc formulations as soon as a new structural theory is developed; whereas, CUF avoids the need for such problem-dependent matrixes via a unified approach based on the use of the expansion functions and indexes τ and s. As the fundamental nucleus of the matrix is derived via the Principle of Virtual Displacements, the order of the structural theory can be changed, and the effect is the use of additional values of the indexes. A detailed explanation of the fundamental nucleus and the assembly of the global stiffness matrix is found in [34].

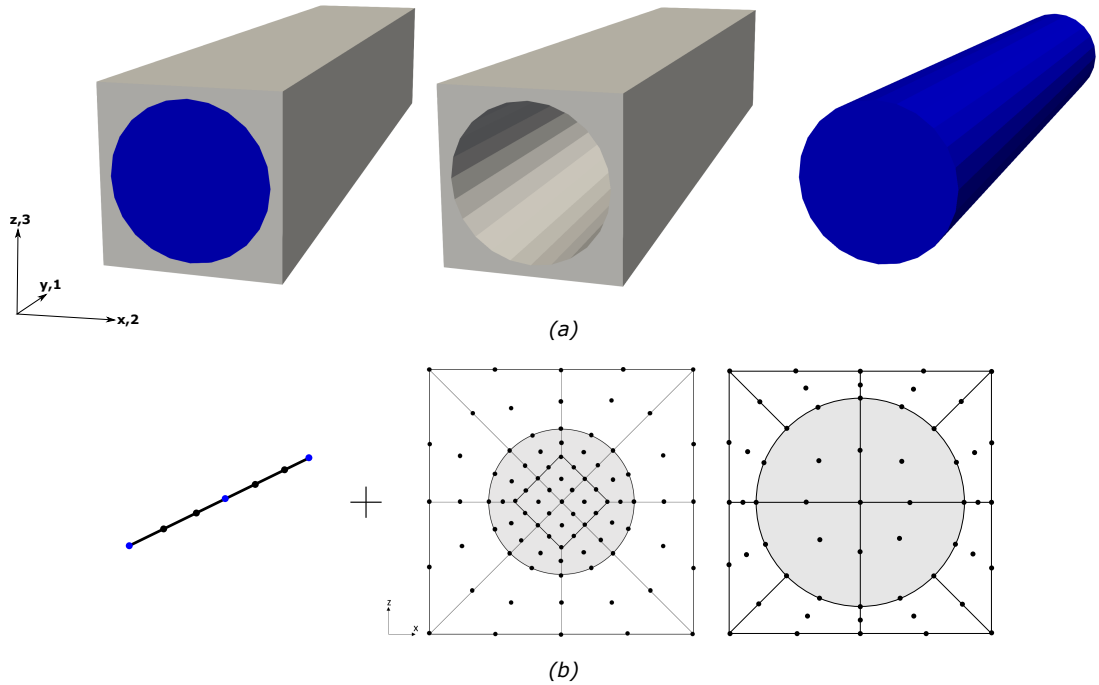

Figure 2: Modelling the RVE using the CW approach. (a) 3D domain of a square-packed RVE and its individual constituents, and (b) 1D-CUF model

3 Component-wise micromechanics framework

The CW micromechanics framework adopts 1D CUF models with Lagrange expansion functions. In this approach, an RVE is modeled, as shown in Fig. 2. Beam elements are used in the RVE thickness direction, and Lagrange expansion elements explicitly model the individual constituents of the RVE cross-section. The formulation is based on the assumption of a periodic microstructure, and periodic boundary conditions (PBC) are applied to the RVE. Such a process ensures the energy equivalence between the heterogeneous material and the effective homogenized medium [9]. The periodic boundary conditions, applied on opposite boundary surfaces, are formulated as

$$u_i^{j+}(x,y,z) - u_i^{j-}(x,y,z) = \bar{\epsilon}_{ik}(x_k^{j+} - x_k^{j-}) \tag{12}$$

where $\bar{\epsilon}_{ik}$ is the applied macroscopic strain, indices $j+$ and $j-$ represent the positive and negative directions, respectively, along x_k. Two PBC sets can thus be distinguished, which are applied in the cross-section edges and the beam ends, respectively, as shown in Fig. 3. The homogenized stress ($\bar{\sigma}_{ij}$)

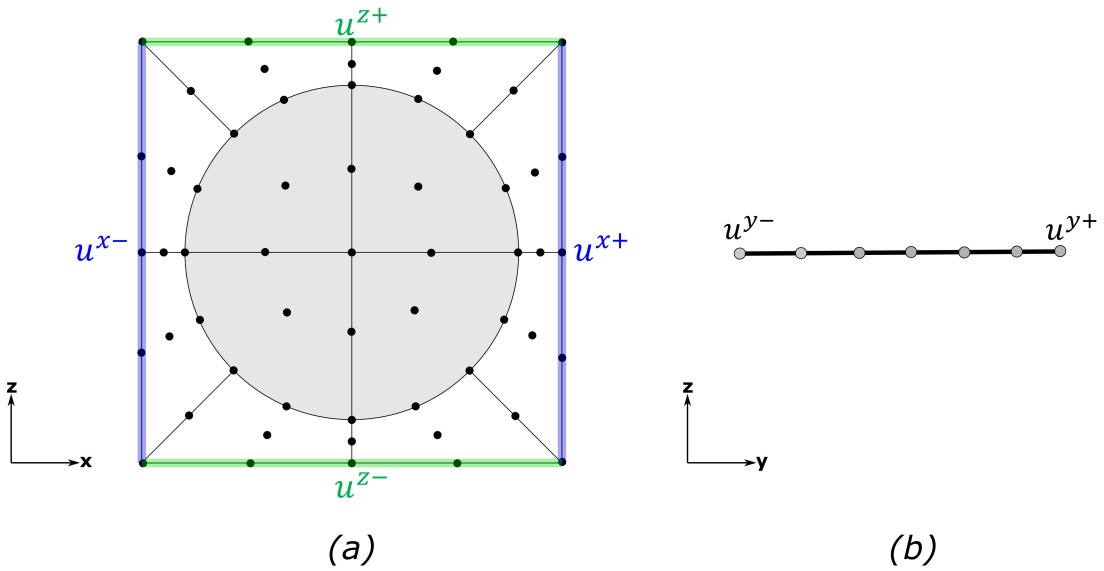

Figure 3: Application of the PBC on a square-packed RVE (a) on the opposite edges of the cross-section and (b) at the beam end nodes

and strain ($\bar{\epsilon}_{ij}$) response is obtained by volume averaging the microscopic fields (σ_{ij}, ϵ_{ij}) [9],

$$\bar{\epsilon}_{ij} = \frac{1}{V}\int_V \epsilon_{ij} dV \tag{13}$$

$$\bar{\sigma}_{ij} = \frac{1}{V}\int_V \sigma_{ij} dV \tag{14}$$

where V is the RVE volume. The constitutive relation for the homogenized medium reads as

$$\bar{\sigma}_{ij} = \bar{C}_{ijkl}\bar{\epsilon}_{ij} \tag{15}$$

where $\bar{C}_{ijkl}$ is the homogenized elastic material matrix. A detailed explanation of the micromechanics framework using the CW approach is given in [31].

Voids are modeled in the matrix constituent of the RVE by selecting a set of Gauss points (GP) within the matrix domain and assigning them arbitrarily low elastic moduli. Such a process creates voids with a domain equal to the volume associated with the selected GP. Matrix GP are iteratively selected as void candidates until the void volume fraction, given as an input, is satisfied. Furthermore, the matrix GP can be selected either randomly throughout the RVE, or be biased in the RVE thickness direction. The former results in voids that are randomly and equally distributed within the RVE, while the latter

results in voids clustered towards one end of the RVE. This methodology thus allows for the development of a fully 3D cubic RVE with matrix voids of a required volume fraction as well as morphology. As an example, a multi-fiber RVE with 1% randomly distributed voids has been schematically shown in Fig. 4. Such a technique enables the efficient development of multiple configurations of the RVE for a given void volume fraction, which is an important requirement for statistical studies on the influence of voids.

The void modeling in this paper exploits the 3D distributions of Gauss points within a beam element. The distribution is 3D because of the superposition of the 1D distribution for the integration of the shape functions and the 2D one of the expansion functions. The localized deformation inside the void is not supported because it would require the explicit modeling of the morphology of the void by inserting a geometrical discontinuity. Such a choice can be made in CUF as can be made in commercial FE via brick elements. Although such a strategy would lead to more accurate local stress distributions, it may be impractical as the number of void increases. It could present some numerical issues due to the modeling of the transition between different scale regions when the size of the void is small compared to the surrounding matrix and fibers.

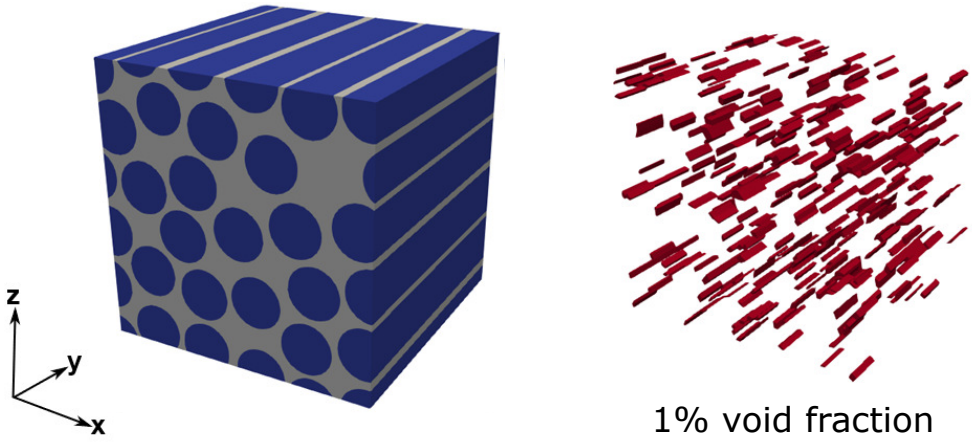

Figure 4: A multi-fibre RVE with 1% voids randomly distributed within the matrix

4 Numerical results

4.1 Mesh convergence study on hex-packed RVE

The current set of numerical assessments comprises an initial study investigating the influence of the mesh on the quality of the homogenized stiffness and micro-stress response, for the case of both pristine

RVE and those with voids, and their convergence characteristics. For simplicity, a hex-packed RVE with a 60% fiber volume fraction is considered, and a series of CUF models are developed with an increasing refinement of the cross-section mesh. The fiber radius is 3.6 μm, and each edge of the cubic RVE has a length of 11.65 μm. The constituent material properties are listed in Table 1, and are obtained from [38]. A schematic representation of the cross-sectional meshes used in the assessment is shown in Fig. 5. For each mesh, two models are developed, with 2 B4 and 4 B4 beam elements along the y-axis. For RVE with voids, the void fraction is kept constant at 2%, and the voids are randomly distributed within the matrix. Micromechanical homogenization is first performed to determine the effective material properties of both types of RVE. The error of the solutions obtained by the various models, for the solution of the most refined model (316 L9-4 B4), is plotted in Fig. 6(a). A dehomogenization procedure is then performed on the RVE, loaded in transverse tension in the x-axis, and the maximum value of the local stress field σ_{xx} is determined. The maximum stresses predicted by the various models are plotted in Fig. 6(b). The following observations are made

- A converged solution is observed for the homogenized elastic properties using the 112 L9 model, as seen in Fig. 6(a). Progressive refinement along the y-axis, keeping the cross-section mesh constant, does not significantly influence the homogenized properties.

- The maximum value of the local stress field, σ_{xx}, approaches a converged value at the same level of mesh refinement (112 L9). Variations in the maximum values in the converged state stem from the randomness of the void morphology. The void modeling approach used in the present work, based on assigning air-like elastic properties to selected matrix integration points, avoids issues of stress singularities, and ensures convergence.

- The rate of convergence, for both homogenized properties and maximum local stresses, follows a similar trend i.e., convergence occurs for the same level of refinement. This is true for pristine RVE as well as RVE with voids.

- The introduction of matrix voids within the RVE does not cause significant changes in the convergence rate and characteristics, compared to the case of the pristine RVE.

Table 1: Properties of the constituent materials [38], the units of the elastic moduli are GPa

Material	E_{11}	$E_{22} = E_{33}$	$G_{12} = G_{13}$	G_{23}	$\nu_{12} = \nu_{13}$	ν_{23}
Fiber	223.987	18.534	36.898	7.232	0.258	0.282
Matrix	3.700	3.700	3.700	3.700	0.400	0.400

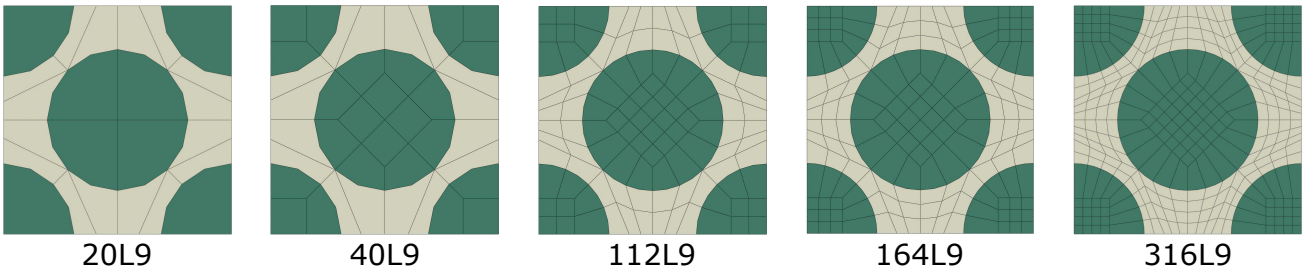

Figure 5: Cross-sectional discretisation used for the hex-packed RVE

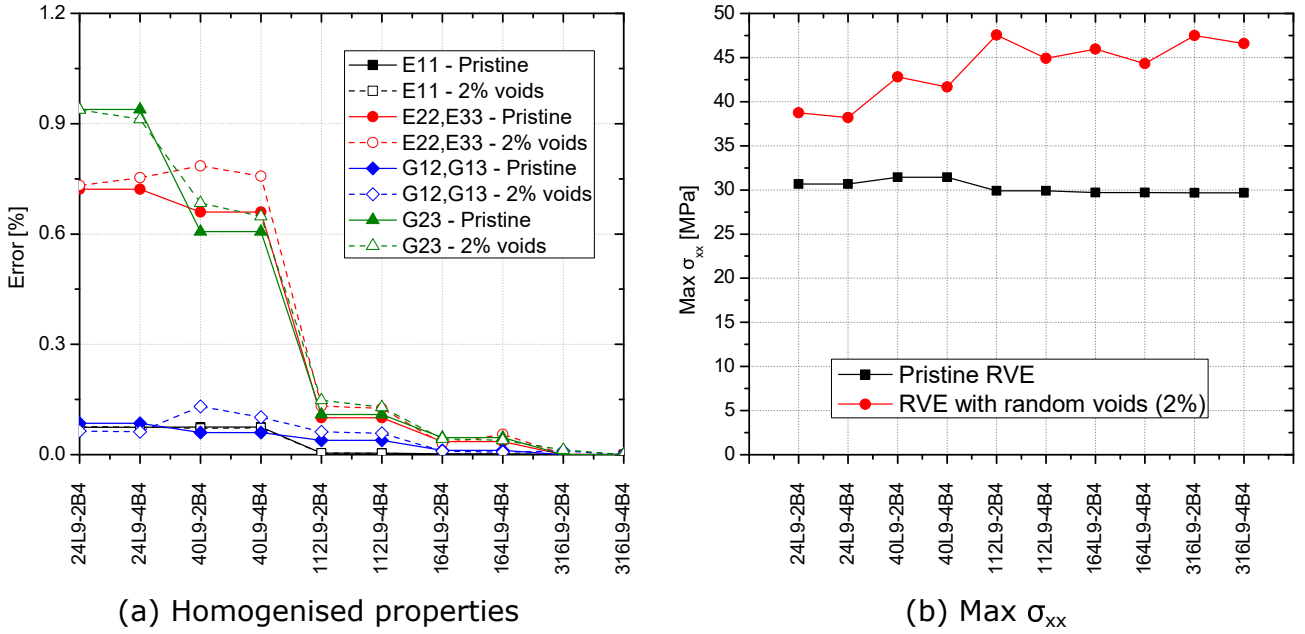

Figure 6: Convergence of homogenised elastic properties and local stress component σ_{xx} with increasing cross-section mesh refinement

4.2 Pristine RVE

The RVE has 22 randomly distributed fibers, and the material system is carbon/epoxy with 60% of fiber volume fraction. Figure 7 shows the randomly distributed fibers; the blue cylinders represent the carbon fibers, and the white portion indicates the matrix. The side of the cross-section is 38.5 µm. The thickness along the y-axis is 19.25 µm. The radius of the fiber is 3.6 µm. The material properties are

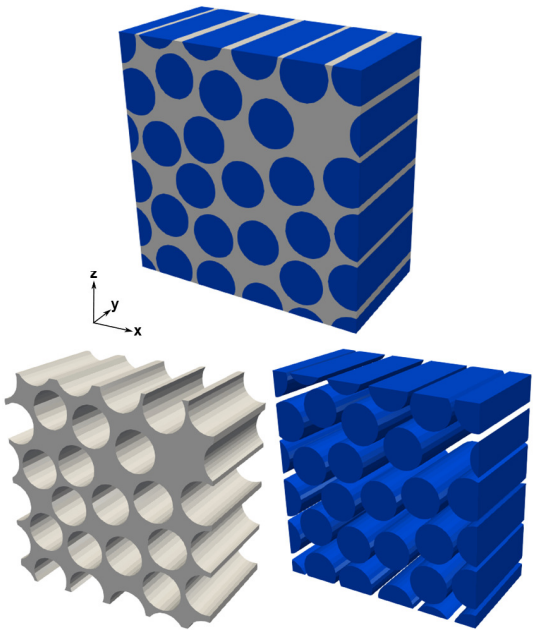

Figure 7: RVE with randomly distributed fibers

in Table 1 and retrieved from Sevenois et al. [38]. The longitudinal direction of the fiber coincides with the y-axis, see Fig. 2. This section aims to evaluate the influence of the cross-section modeling on the homogenized properties and select the discretization for all subsequent analyses. Figures 8 show two examples of cross-section discretizations. The FE mesh along y is constant and has one B4 element; as shown in previous works [31, 32], such axial mesh is sufficiently accurate. Figure 9 shows the homogenized properties for various meshes. The reference value to compute the error is the one provided by the most refined discretization, 3144 L9. The coarsest discretization has the highest error. However, such errors are lower than 2%. Given that the use of the 314 L9 leads to a considerably reduced computational cost for the statistical studies, the following numerical examples will use the same discretization. The similar convergence trends observed in Section 4.1, for both homogenized properties and maximum local stress fields, verify the suitability of the 314 L9 model for the accurate evaluation of the local stress fields for the current numerical assessment. A further assessment focuses on the verification of the results via

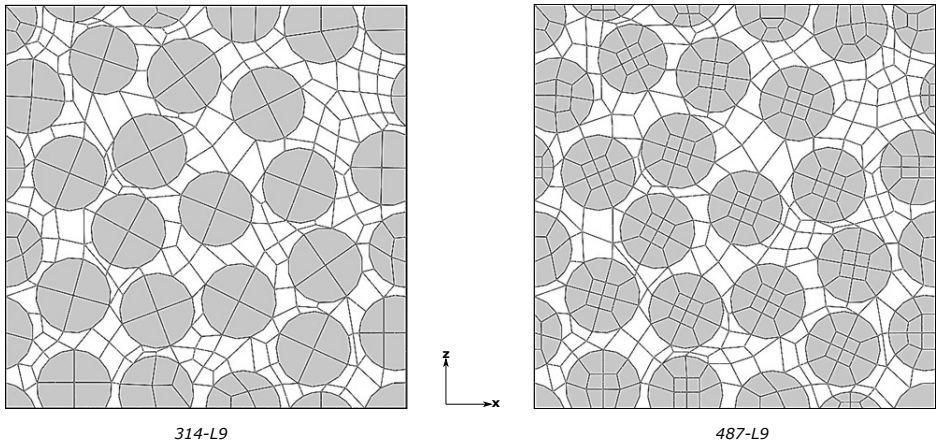

Figure 8: Cross-sections with 314 and 487 L9 elements

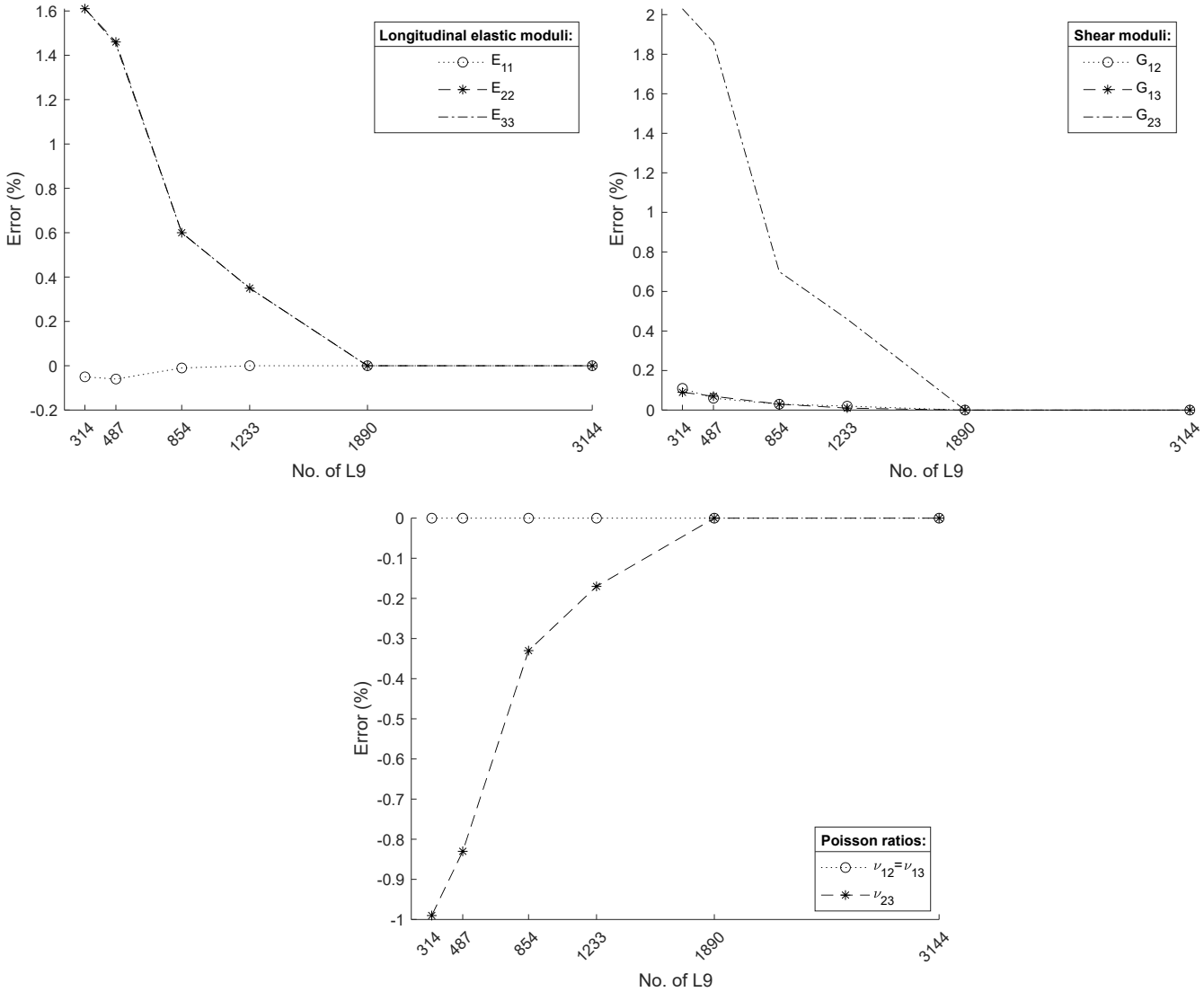

Figure 9: Effect of the cross-section discretization on the homogenized properties of the pristine RVE

a comparison with [38], see Table 2. The results show a good match. Figures 10 and 11 show stress distributions given by an applied strain of 0.2%.

Table 2: Homogenized properties for the pristine RVE via 314 L9 and results from [38], the units of the elastic moduli are GPa

Model	1D-CUF	FE ref. [38]
E_{11}	135.88	135.74
E_{22}	9.96	9.66
E_{33}	9.91	9.66
G_{12}	5.19	5.31
G_{13}	5.02	5.31
G_{23}	3.15	3.23
ν_{12}	0.31	0.31
ν_{13}	0.31	0.31
ν_{23}	0.47	0.48

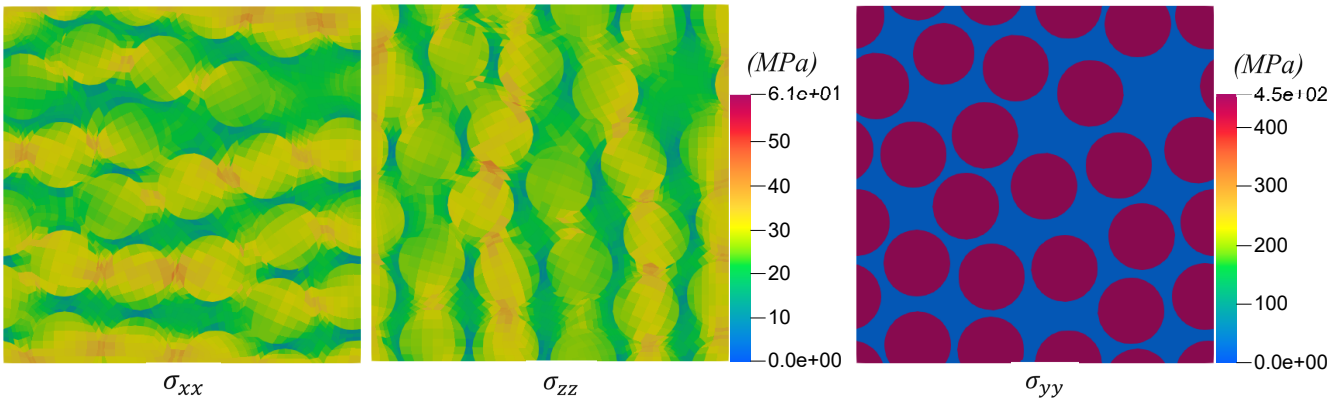

Figure 10: Axial stress contours, σ_{xx}, σ_{zz}, and σ_{yy}, with applied ϵ_{xx}, ϵ_{zz}, and ϵ_{yy}, respectively, pristine RVE

4.3 RVE with voids

The analysis of voids considers two RVE configurations. The first one - referred to as RVE-1, has the same material and geometrical characteristics seen in the previous section. The second one, RVE-2, differs only for the dimension along y; that is, 38.5 µm. From the modeling standpoint, the cross-section discretizations are the same, whereas two B4 are employed in RVE-2. Figure 12 shows both RVE and the beam meshes in which the reported mesh over the matrix is not representative of the numerical model, but it serves postprocessing purposes. Table 3 summarizes the main characteristics of the models. The shape and void percentages considered in this paper are consistent with those from the literature [8]. The analysis considers two void distributions as follows

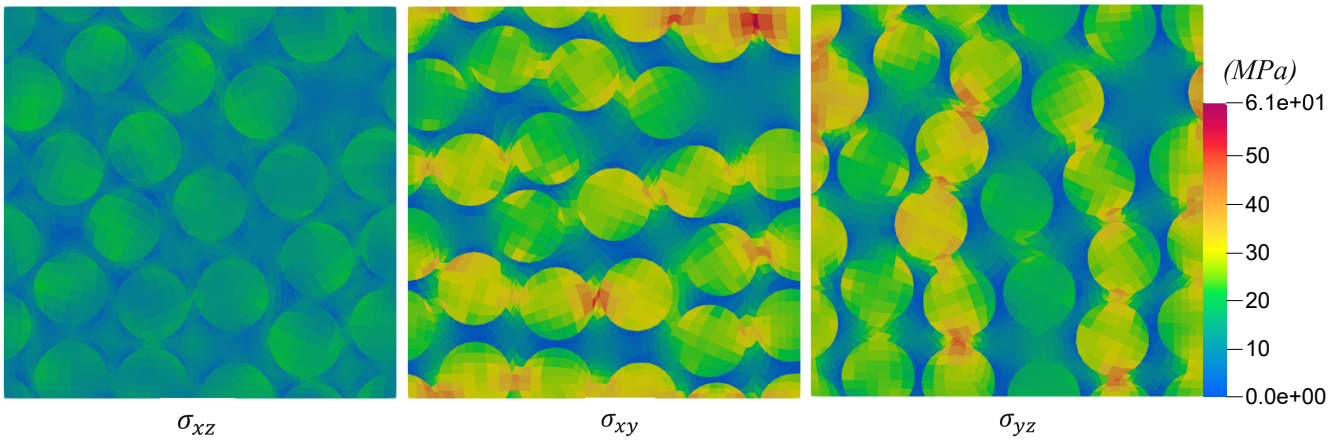

Figure 11: Shear stress contours, σ_{xz}, σ_{xy}, σ_{yz}, with applied ϵ_{xz}, ϵ_{xy}, and ϵ_{yz}, respectively, pristine RVE

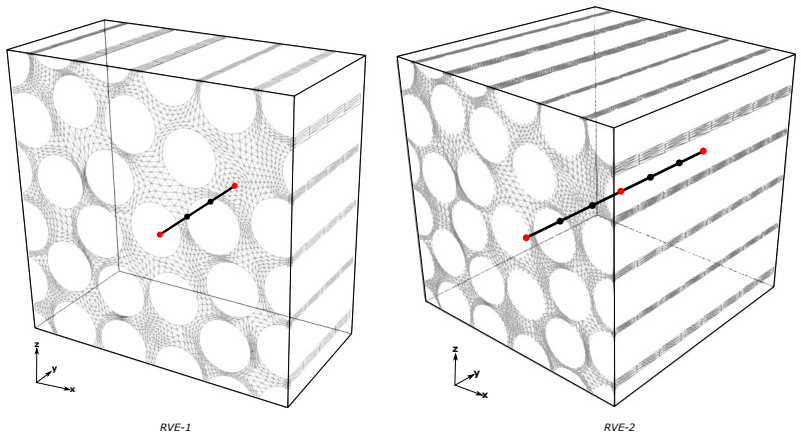

Figure 12: RVE-1 and RVE-2 and beam meshes

- The first distribution - referred to as VD-1 - is random within the RVE. Figure 13 shows an example of this void arrangement for the RVE-2.

- The second distribution - referred to as VD-2 - is random along the cross-section but follows a linear distribution of the void percentage along y. By considering Fig. 14, the first segment along y has 5% of the total voids, while the last one has some 30%. The aim is to simulate a configuration with moderate clustering.

In both cases, 100 distributions per each void volume fraction were considered to evaluate statistical parameters. Table 4 presents the main characteristics of each distribution. VD-2 was applied only to RVE-2 due to the small y-dimension of RVE-1. Furthermore, VD-2 considers the random variation of the slope of the distribution; that is, the maximum of voids can be either on the last segment or the first

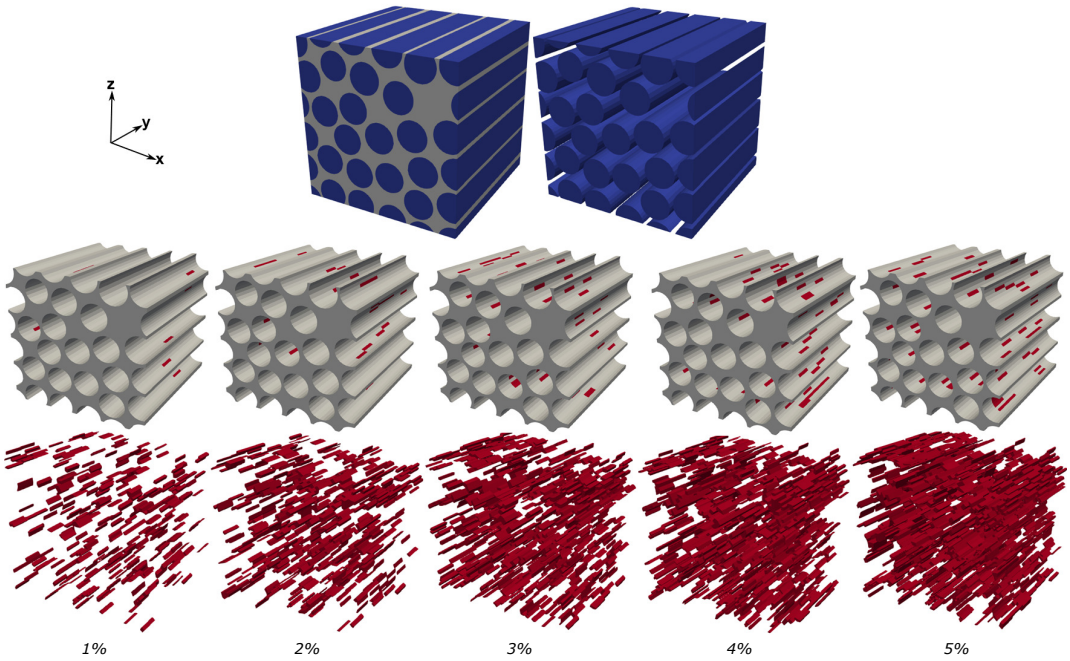

Figure 13: Random distributions of voids with increasing contents, VD-1

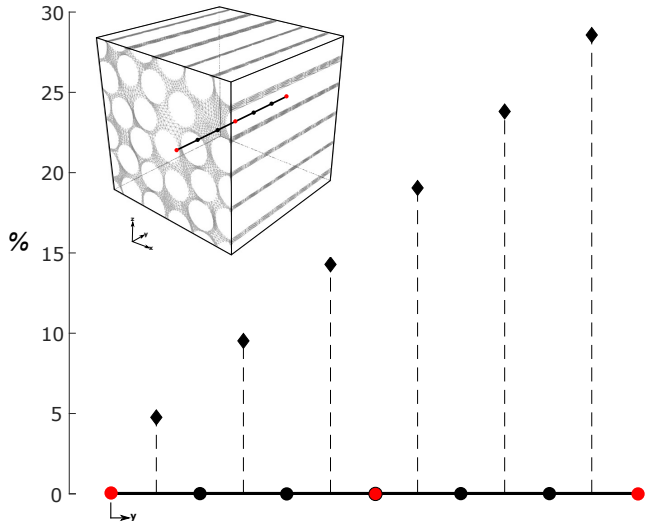

Figure 14: Clustering of voids, VD-2

Table 3: Structural and FE modeling of RVE-1 and RVE-2

	Discretization	DOF
RVE-1	314 L9 on the cross-section, one B4 along y	15876
RVE-2	314 L9 on the cross-section, two B4 along y	27783

one. The results consider homogenized properties and local distributions of stress. For the latter, all six

Table 4: Summary of VD-1 and VD-2

VD-1	
RVE considered	RVE-1 and RVE-2
Void volume fractions	1, 2, 3, 4, 5 %
Subcases per void volume fractions	100
VD-2	
RVE considered	RVE-2
Void volume fractions	1, 2, 3, 4, 5 %
Subcases per void volume fractions	100

strains were applied separately, and, in each case, the strain is 0.2%. The statistical parameters employed are the following [39, 40]: mean value $\bar{x}$, median q_2, standard deviation s, minimum value min, maximum value max, first quartile q_1, third quartile q_3. Such parameters were computed on the maximum values of stress components of a given void distribution and content.

4.3.1 Influence of void distribution on homogenized properties

The first numerical assessment focuses on the homogenized properties. Tables 5 and 6 present the results regarding VD-1 and both RVE. Table 7 shows the results for RVE-2 and considering VD-2. The results suggest the following:

- As expected, the void content affects the mechanical properties with the degradation that can reach 4%. The standard deviation is very low in all cases.
- The use of a deeper RVE does not affect the mean values; that is, there is no significant influence on the homogenized properties. Likewise, the adoption of different void distributions does not lead to significant modifications of the properties.
- The influence of RVE and void content on the standard deviation is more evident, but, in all cases, s is low.

Table 5: Mean value ($\bar{x}$) and standard deviation (s) of the homogenized properties, RVE-1 and VD-1

		Void content (%)				
		1	2	3	4	5
$\bar{x}$ (GPa)	E_{11}	135.846	135.809	135.771	135.734	135.697
	E_{22}	9.887	9.818	9.747	9.679	9.609
	E_{33}	9.836	9.765	9.695	9.625	9.555
	G_{12}	5.156	5.127	5.098	5.069	5.040
	G_{13}	4.993	4.964	4.935	4.906	4.877
	G_{23}	3.125	3.102	3.080	3.057	3.034
s (MPa)	E_{11}	0.744	1.100	1.056	1.258	1.460
	E_{22}	2.641	3.425	3.480	3.755	4.471
	E_{33}	2.264	2.735	3.388	4.493	3.960
	G_{12}	1.869	2.132	2.508	2.733	3.039
	G_{13}	1.496	1.956	2.502	2.923	2.828
	G_{23}	0.571	0.953	0.887	1.026	1.316

Table 6: Mean value ($\bar{x}$) and standard deviation (s) of the homogenized properties, RVE-2 and VD-1

		Void content (%)				
		1	2	3	4	5
$\bar{x}$ (GPa)	E_{11}	135.846	135.809	135.772	135.734	135.697
	E_{22}	9.887	9.818	9.749	9.679	9.609
	E_{33}	9.836	9.766	9.696	9.625	9.555
	G_{12}	5.156	5.127	5.098	5.069	5.040
	G_{13}	4.993	4.964	4.935	4.906	4.878
	G_{23}	3.125	3.103	3.080	3.057	3.034
s (MPa)	E_{11}	0.508	0.680	0.784	0.850	0.963
	E_{22}	1.470	2.174	2.231	2.910	3.108
	E_{33}	1.307	2.036	2.761	2.405	3.127
	G_{12}	1.064	1.673	1.835	1.979	2.064
	G_{13}	0.969	1.304	1.894	1.790	2.165
	G_{23}	0.456	0.580	0.647	0.790	0.868

Table 7: Mean value ($\bar{x}$) and standard deviation (s) of the homogenized properties, RVE-2 and VD-2

		Void content (%)				
		1	2	3	4	5
$\bar{x}$ (GPa)	E_{11}	135.846	135.809	135.772	135.734	135.697
	E_{22}	9.887	9.818	9.749	9.679	9.610
	E_{33}	9.836	9.766	9.696	9.625	9.555
	G_{12}	5.156	5.127	5.098	5.069	5.040
	G_{13}	4.994	4.964	4.936	4.906	4.877
	G_{23}	3.125	3.103	3.080	3.057	3.034
s (MPa)	E_{11}	0.511	0.682	0.686	0.825	0.919
	E_{22}	1.566	1.955	2.330	2.680	2.527
	E_{33}	1.540	2.047	2.339	2.692	2.794
	G_{12}	1.120	1.448	1.765	1.824	1.921
	G_{13}	1.064	1.194	1.585	1.816	1.970
	G_{23}	0.417	0.573	0.658	0.771	0.936

4.3.2 Influence of void distribution on stress fields

The second numerical assessment concerns the influence of RVE and VD on the stress distributions. Table 8 shows the statistical parameters regarding the maximum values of axial stress found in the RVE-1 having VD-1 and under various axial strains. The first column indicates the applied strain, the second one the stress component, whereas the last one shows the void content. Similarly, Table 9 presents the statistical parameters obtained by applying shear strains. Figure 15 shows the box plots of the RVE-1 with VD-1 and applied axial strains. The most relevant stress components are reported. The box plot displays simultaneously several features of the data set [40]. The left side of the box is the first quartile (q_1), and the right side is the third quartile (q_3). The difference $q_3 - q_1$ is the interquartile range (IQR). The vertical line inside the box is the second quartile or median (q_2). The dashed horizontal line on the left of the box connects q_1 to the smallest data point within 1.5 IQR. Similarly, the one on the right side connects q_3 to the largest data point within 1.5 IQR. Data points falling beyond these ranges are indicated explicitly. For example, considering the case of 5% voids and ϵ_{xx} for RVE-1, the highest maximum stress is 106.8 MPa. q_1, q_2 and q_3 are 72.6, 77.6 and 84 MPa, respectively. The lowest minimum of stress is 62.8 MPa. Figures 16, 17, and 18 are the box plots with applied shear strains for RVE-1 and both strains for RVE-2.

The results of VD-2 are in Figures 19 and 20. Figure 21 shows an example of stress distributions over a cross-section of the RVE. The cross-sections are those in which the peak values were found. The results suggest the following

- There is a general increase of stresses moving from RVE-1 to RVE-2 and VD-1 to VD-2. In other words, by considering deeper RVE and clustering, higher stresses were found.

- By considering Fig. 21, it can be seen how the locations of stress peaks are in the proximities of the interface between fibers and matrix. Moreover, according to the void distributions related to Fig. 21, the location of the peaks coincides with a void interface.

- The increase of void content leads to higher stresses and wider stress ranges. Several box plots show rightward skewness of the data, i.e., quite high-stress peaks as compared to the mean value.

- By considering Table 8, it can be seen that, by applying a longitudinal strain (ϵ_{yy}), most of the load is carried by the fibers as shown by the high values of σ_{yy}. Figures 15 and 17 show how the increase of the void content, i.e., the deterioration of the matrix, causes a slight increase in fiber stress.

Table 8: Statistical parameters of the axial stresses (MPa) for various void contents (%) with applied ϵ_{xx}, ϵ_{yy}, and ϵ_{zz}, RVE-1 and VD-1

		$\bar{x}$	q_2	s	min	max	q_1	q_3	Voids
ϵ_{xx}	σ_{xx}^{max}	56.670	56.197	4.841	47.949	75.549	53.463	59.128	1
		63.619	62.368	6.083	53.205	83.828	59.979	67.256	2
		67.209	66.043	6.359	57.859	93.672	62.654	69.749	3
		72.385	71.975	6.880	60.132	93.625	67.939	76.037	4
		78.668	77.614	8.927	62.752	106.830	72.615	84.004	5
	σ_{yy}^{max}	37.084	36.600	3.283	30.820	49.030	35.126	39.027	1
		41.574	40.554	4.313	34.638	56.720	38.633	44.150	2
		43.947	43.016	4.106	35.976	60.923	41.084	45.546	3
		47.270	46.986	4.529	38.287	60.974	44.018	49.376	4
		51.387	50.242	6.131	40.111	71.246	47.215	55.293	5
	σ_{zz}^{max}	36.775	36.527	3.384	29.576	48.887	34.566	38.607	1
		41.407	40.373	4.579	34.433	58.128	37.979	44.188	2
		43.690	42.999	4.356	36.284	59.424	40.579	45.822	3
		46.611	46.085	4.604	38.434	60.719	43.152	49.202	4
		50.750	49.705	6.247	39.652	71.785	46.245	54.809	5
ϵ_{yy}	σ_{xx}^{max}	21.365	21.054	1.711	18.488	26.995	20.335	21.940	1
		24.380	23.896	2.536	20.487	33.686	22.556	25.751	2
		26.259	25.687	2.712	21.732	38.296	24.671	26.999	3
		27.632	27.079	2.638	23.758	38.414	25.733	28.771	4
		30.354	29.779	3.658	23.973	45.779	27.550	32.587	5
	σ_{yy}^{max}	456.784	456.729	0.793	455.612	459.420	456.152	457.119	1
		457.711	457.614	1.069	456.125	461.168	456.913	458.224	2
		458.522	458.341	1.130	456.457	462.539	457.818	459.155	3
		459.116	458.877	1.216	456.268	462.540	458.293	459.875	4
		459.767	459.580	1.315	457.277	463.191	458.828	460.451	5
	σ_{zz}^{max}	21.686	21.250	1.772	18.776	26.737	20.321	22.931	1
		25.415	24.498	3.936	20.010	43.822	22.755	26.549	2
		27.733	26.797	4.229	22.349	44.956	24.731	29.240	3
		29.762	28.635	4.343	23.900	44.237	26.767	31.276	4
		31.531	30.300	4.508	25.207	46.899	28.297	33.226	5
ϵ_{zz}	σ_{xx}^{max}	37.967	37.228	3.636	30.741	49.088	35.709	39.420	1
		43.580	41.379	7.155	35.145	80.370	39.059	46.015	2
		47.999	46.647	7.202	35.386	72.759	43.037	50.447	3
		51.617	48.708	8.836	39.474	81.787	45.579	55.250	4
		53.271	51.648	8.195	39.851	79.988	47.618	56.238	5
	σ_{yy}^{max}	38.673	38.031	3.561	32.136	50.242	36.481	40.160	1
		44.237	42.425	7.075	36.116	79.411	39.652	46.604	2
		48.770	47.737	7.144	37.803	75.340	43.465	52.086	3
		52.709	50.127	8.716	41.658	79.996	47.246	55.247	4
		54.410	52.991	8.124	41.642	83.652	48.430	58.174	5
	σ_{zz}^{max}	59.310	58.232	5.392	50.047	76.481	56.026	61.267	1
		67.781	65.093	10.457	54.467	118.228	60.751	71.349	2
		74.608	72.414	10.733	60.051	115.875	66.339	79.398	3
		80.906	77.128	13.076	61.675	122.699	73.160	84.118	4
		83.825	81.378	11.946	63.852	129.370	75.342	89.852	5

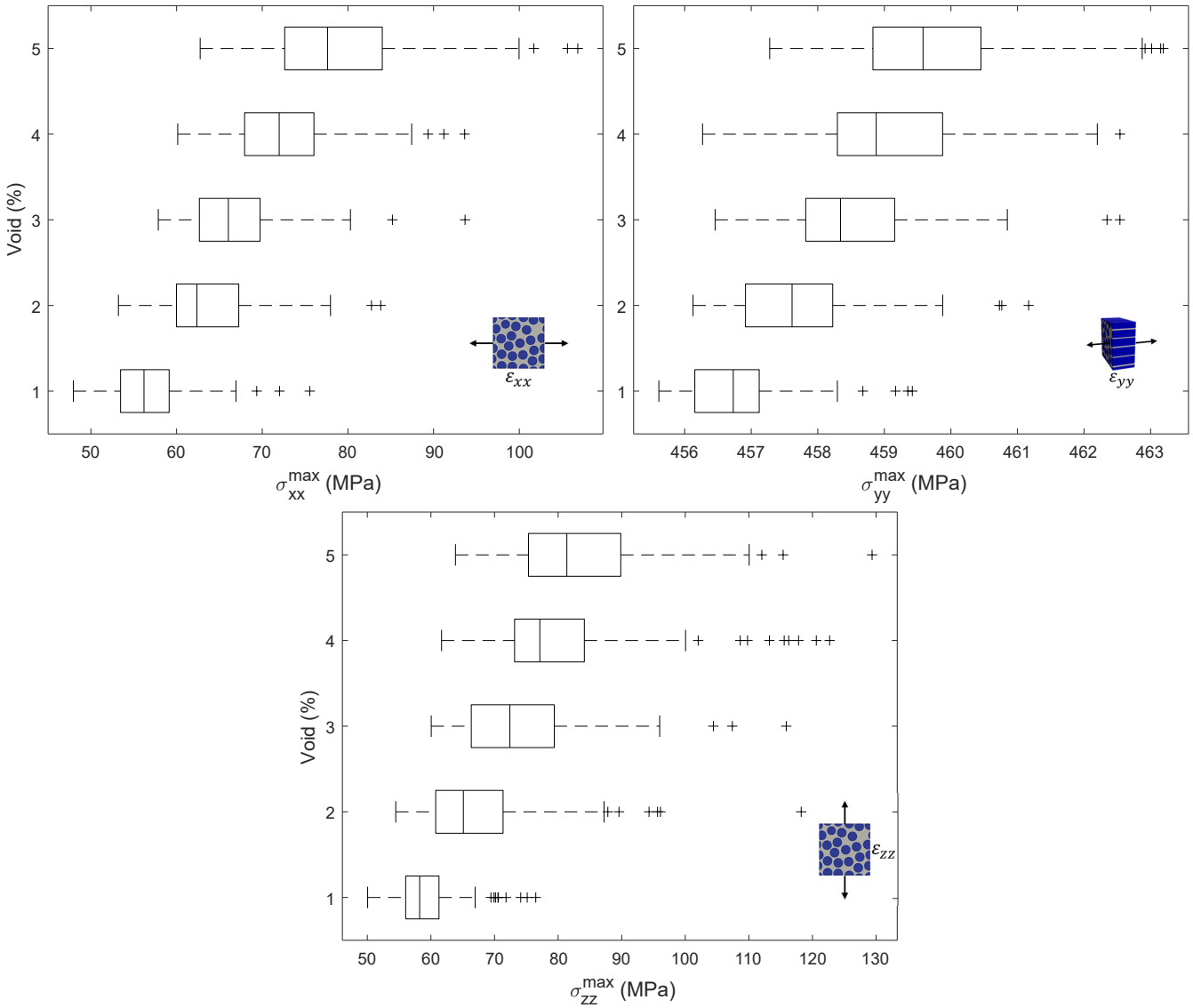

Figure 15: Box plots of axial stresses with applied axial strains, RVE-1 and VD-1

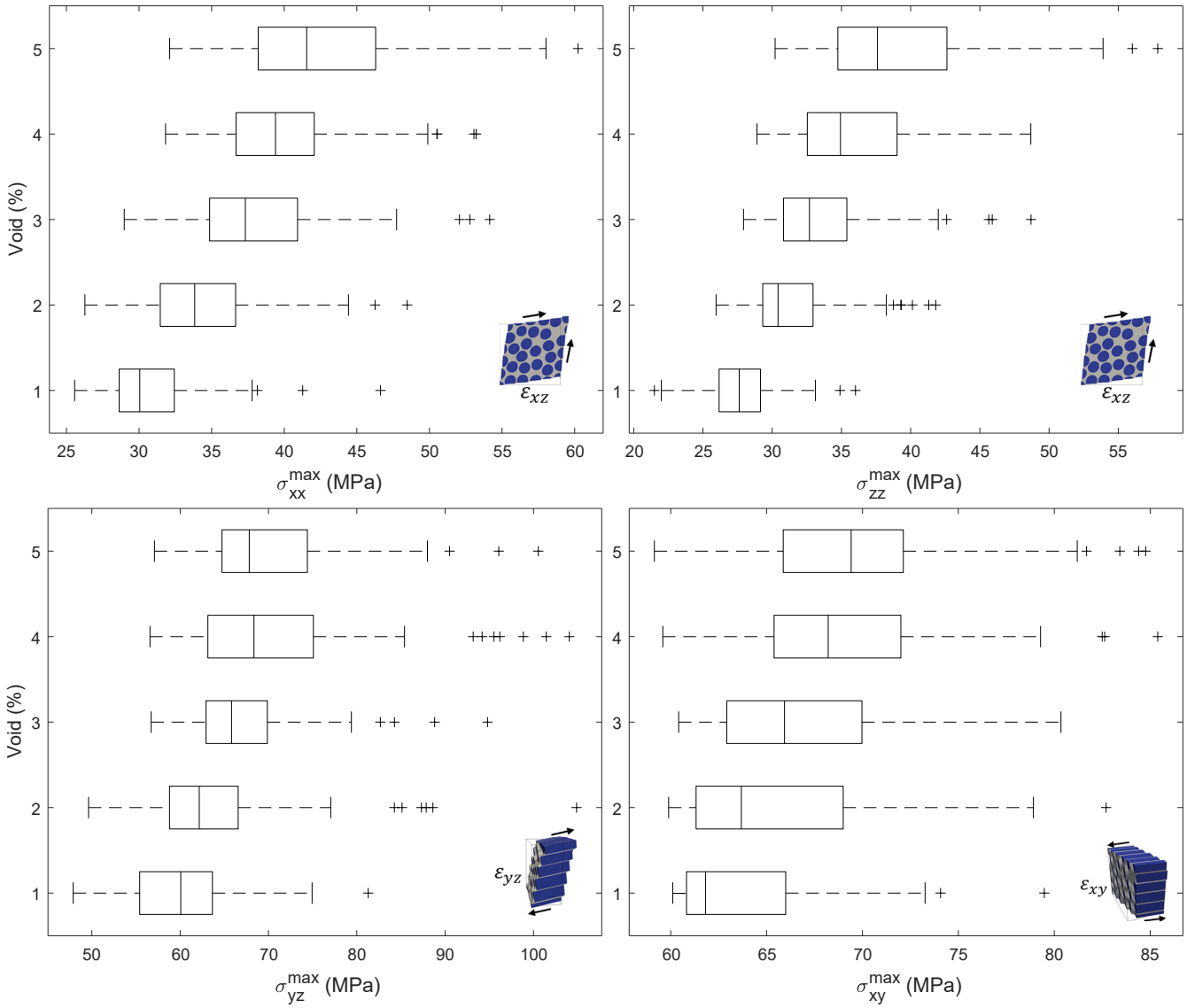

Figure 16: Box plots of stress components with applied shear strains, RVE-1 and VD-1

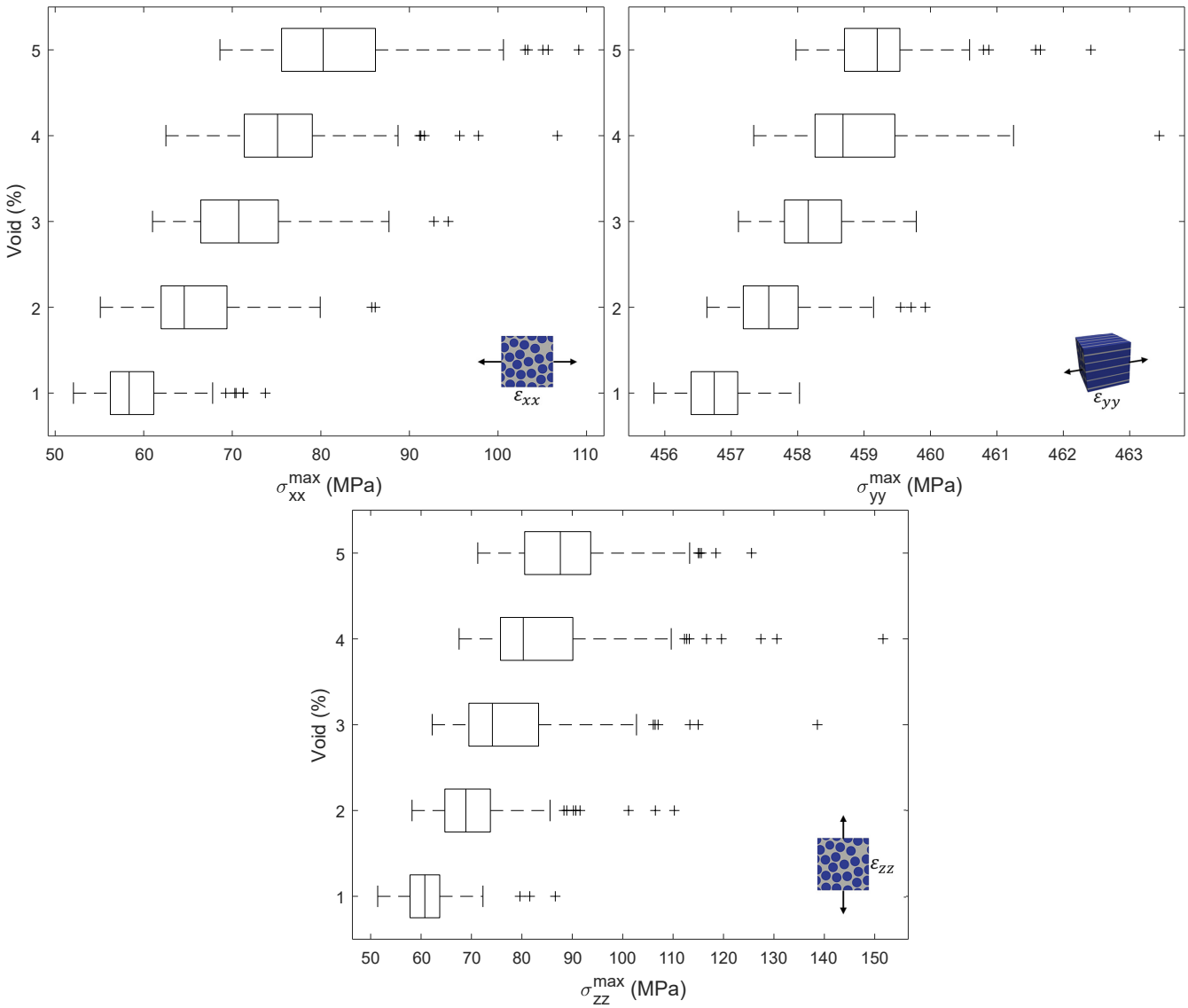

Figure 17: Box plots of axial stresses with applied axial strains, RVE-2 and VD-1

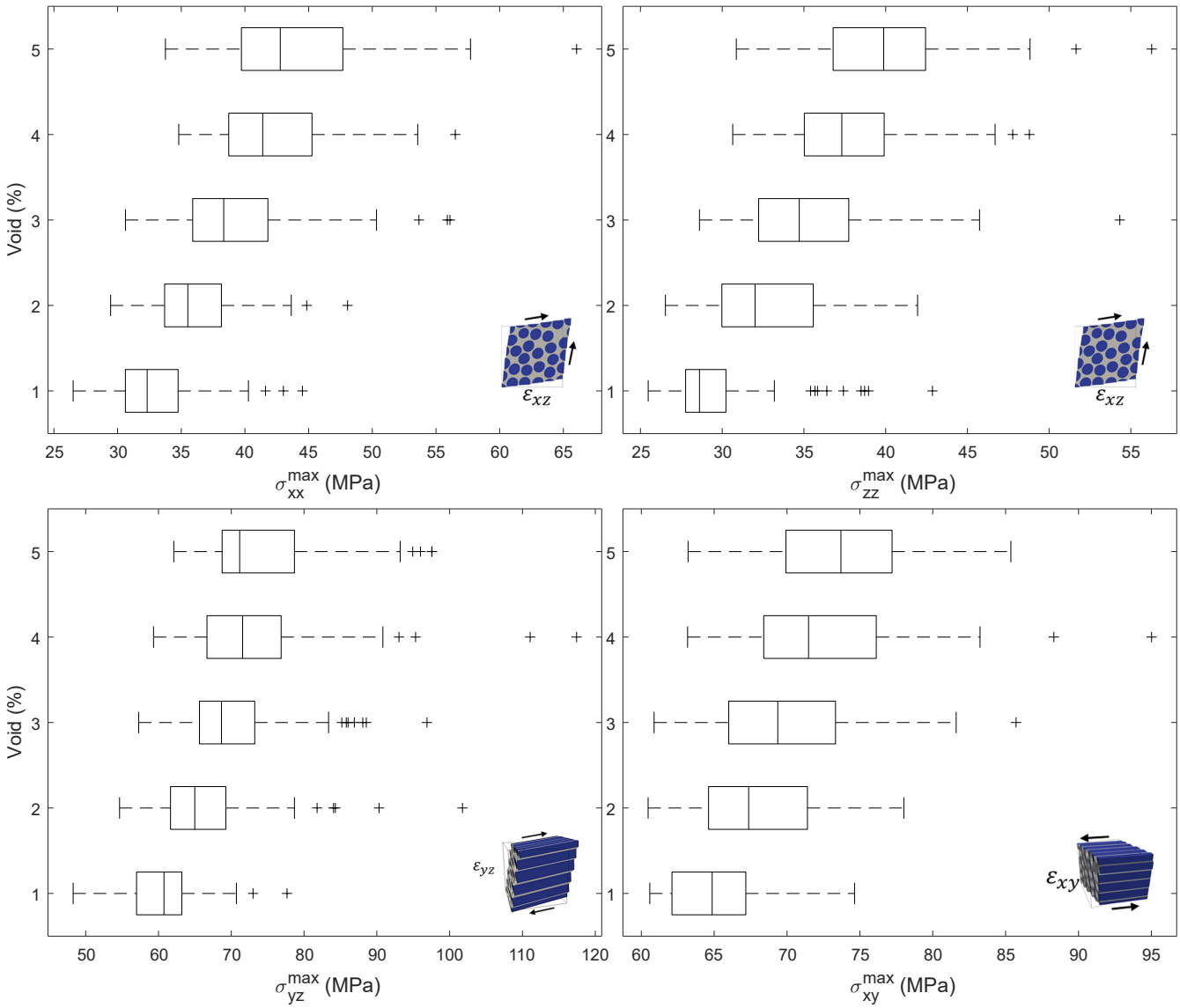

Figure 18: Box plots of stress components with applied shear strains, RVE-2 and VD-1

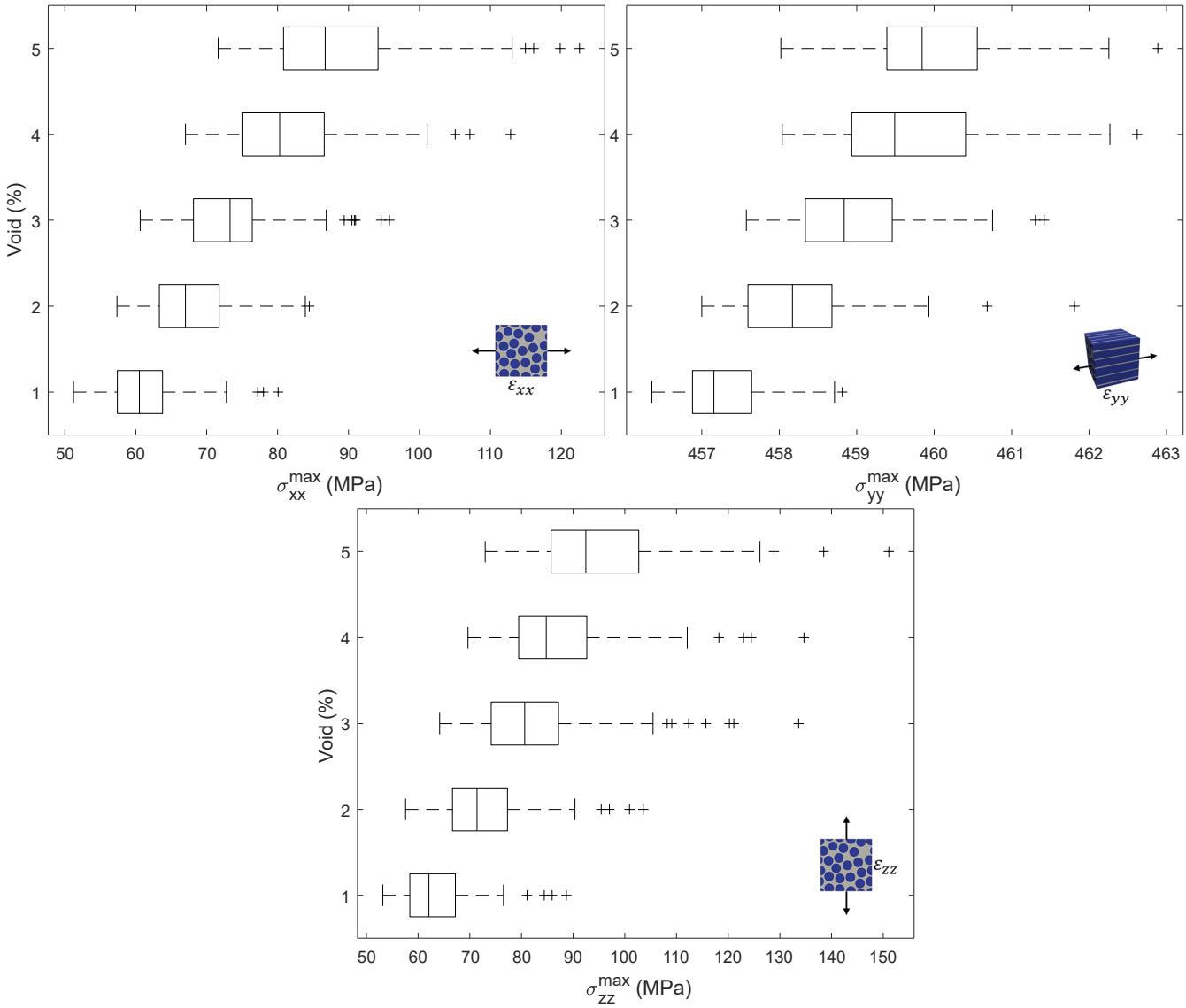

Figure 19: Box plots of stress components with applied axial strains, RVE-2 and VD-2

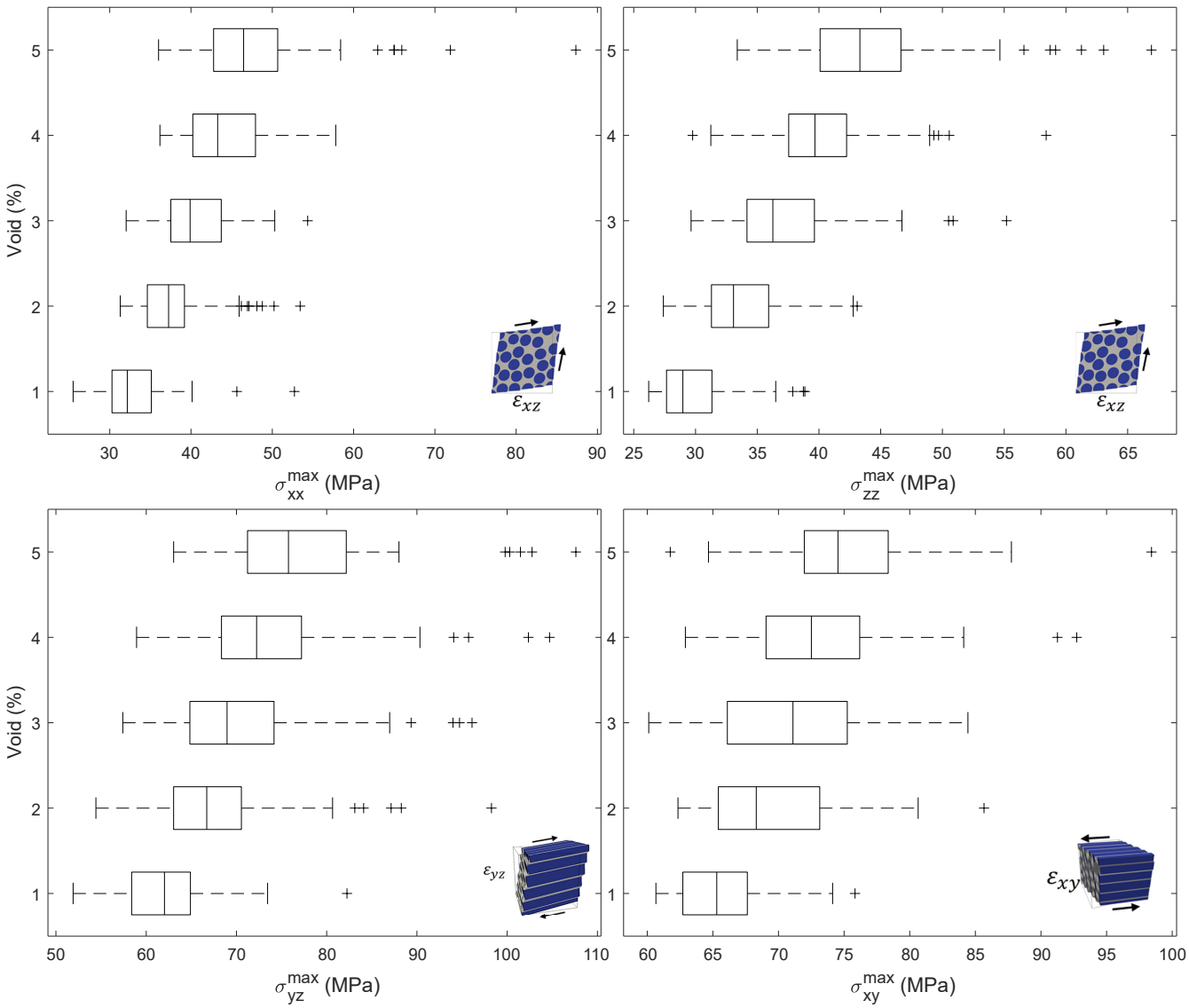

Figure 20: Box plots of stress components with applied shear strains, RVE-2 and VD-2

Table 9: Statistical parameters of stresses (MPa) for various void contents (%) with applied ϵ_{xz}, RVE-1 and VD-1

	$\bar{x}$	q_2	s	min	max	q_1	q_3	Voids
	30.805	30.050	3.415	25.565	46.629	28.635	32.427	1
	34.537	33.835	4.170	26.272	48.472	31.461	36.653	2
σ_{xx}^{max}	38.093	37.324	5.138	28.982	54.148	34.863	40.916	3
	39.908	39.397	4.557	31.828	53.213	36.679	42.068	4
	42.705	41.544	5.721	32.111	60.232	38.208	46.298	5
	22.234	22.371	2.278	18.175	31.514	20.228	23.627	1
	25.130	24.513	2.889	20.277	35.152	23.448	26.018	2
σ_{yy}^{max}	27.535	27.161	3.586	21.789	38.993	25.277	29.220	3
	29.044	28.498	3.446	22.878	39.533	26.713	30.997	4
	31.553	30.680	4.652	23.472	46.079	28.268	34.002	5
	27.696	27.621	2.648	21.492	36.014	26.165	29.158	1
	31.258	30.426	3.326	25.948	41.815	29.317	32.955	2
σ_{zz}^{max}	33.543	32.692	4.062	27.929	48.693	30.819	35.393	3
	35.801	34.934	4.262	28.906	48.680	32.539	39.023	4
	39.403	37.604	6.398	30.211	57.848	34.744	42.619	5
	23.332	22.787	1.310	22.086	30.339	22.477	23.749	1
	25.533	24.852	2.831	22.225	35.063	23.441	26.449	2
σ_{xz}^{max}	25.883	25.173	2.420	22.469	33.916	24.117	27.093	3
	27.396	26.760	3.137	23.077	38.418	24.836	28.798	4
	28.870	28.518	3.390	23.295	39.246	26.260	31.173	5

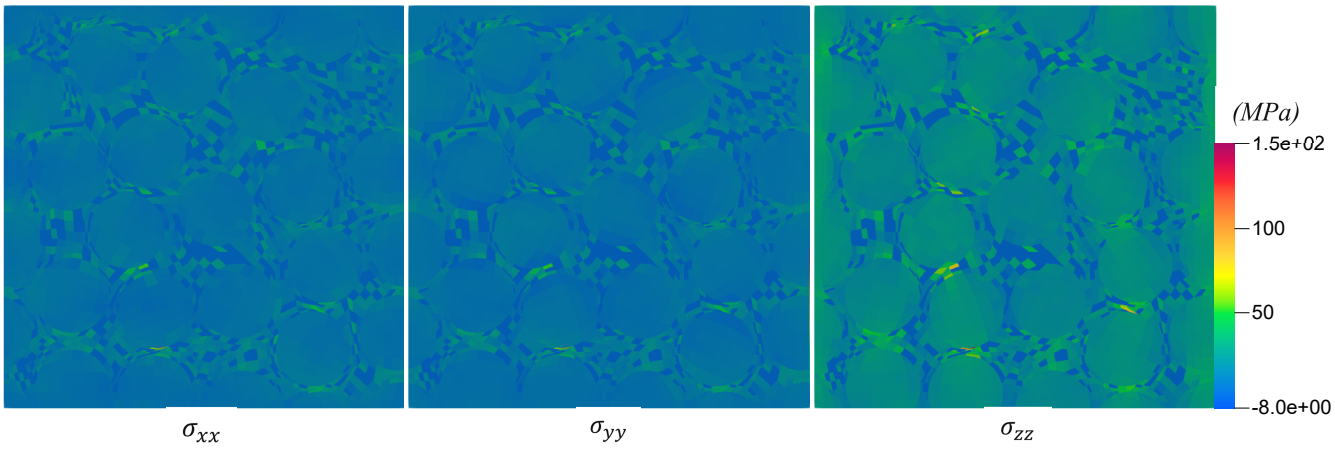

Figure 21: Cross-section distributions of stresses in which peak values were found, void content 5%, applied ϵ_{zz}, RVE-2 and VD-2

- σ_{xx} and σ_{zz} is the stress component with the highest values in the matrix. In some cases, the increase of this component reached three times the value of the pristine RVE.

Further analyses can make use of the probability density function [39] as shown in Figs. 22 and 23. The aim is to show the major differences in the results stemming from the three modeling approaches, namely, RVE-1 and VD-1, RVE-2 and VD-1, and RVE-2 and VD-2. As stated above, there is an increase in both the mean and peak values as deeper RVE and clustering are considered. By moving from RVE-1/VD-1 to RVE-2/VD-2, the mean values increased by some 10%.

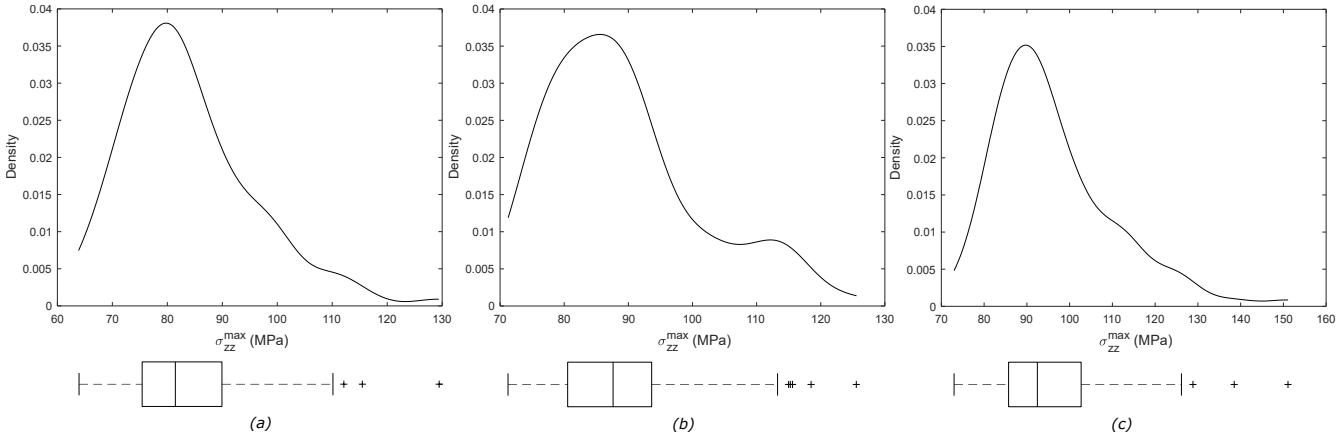

Figure 22: Fitting of the probability density function of σ_{zz}^{max} with applied ϵ_{zz} (a) RVE-1 and VD-1, (b) RVE-2 and VD-1, (b) RVE-2 and VD-2, void content 5%

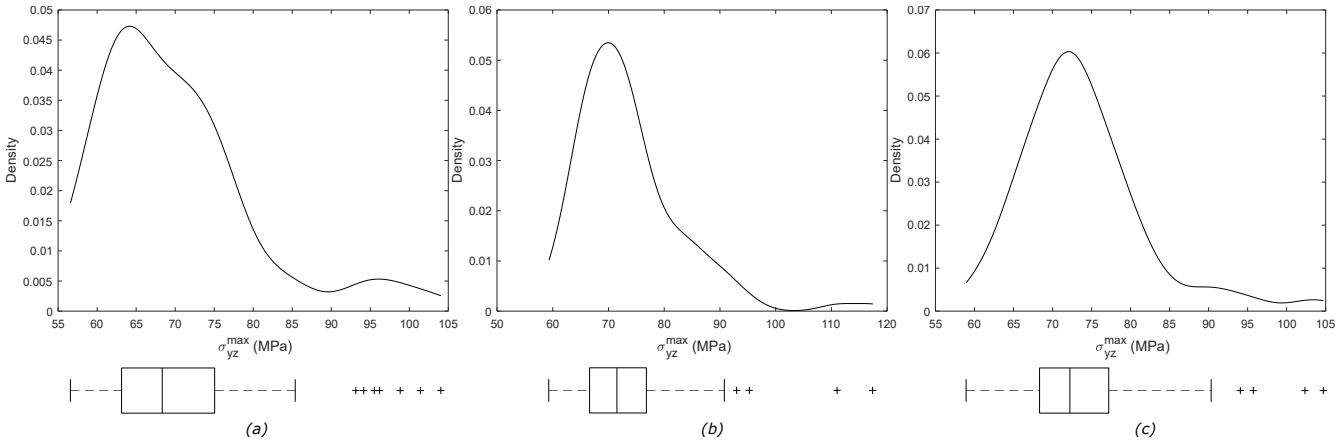

Figure 23: Fitting of the probability density function of σ_{yz}^{max} with applied ϵ_{yz} (a) RVE-1 and VD-1, (b) RVE-2 and VD-1, (b) RVE-2 and VD-2, void content 4%

5 Conclusions

The present work has investigated the influence of matrix voids on the prediction of the homogenized properties and stress fields in RVE for fiber-reinforced polymer composites. The assessments are numerical and based on a numerically efficient FE framework and refined 1D structural models from CUF. The RVE models have randomly distributed fibers and voids within the matrix. Fibers and matrix are modeled via a component-wise approach via Lagrange polynomials defining the displacement field and the geometry; the void modeling exploits the 3D distributions of Gauss points within a beam element, and a selected amount of matrix integration points are prescribed negligible elastic properties. The use of 1D models avoids the aspect ratio constraints of 3D FE and leads to significantly lower computational costs. The present framework can deal with various sets of void distributions to investigate the influence of void content and morphology. Such analyses considered multiple scenarios and statistical metrics. The RVE is 3D, and the influence of its depth is another assessed parameter. The most significant findings are the following:

- As well-known, the influence of void distributions and RVE dimensions on the homogenized properties is low. The void content is the fundamental parameter to consider, independently of the void arrangement.
- The void arrangement influences the stress fields. The clustering of voids leads to higher stress mean values and peaks, and broader ranges of stress.
- Likewise, deeper RVE leads to higher maximum stress values. The combined effect - deeper RVE and clustering - may lead to some 10% increments in the mean values of stress. Such a result may be a warning regarding the proper choice of the RVE geometry to ensure its representativeness concerning stress distributions.
- All six stress components are affected with particularly significant variations in cross-sectional axial components.

The future extensions should consider the nonlinear analysis to investigate the influence of voids on failure. Furthermore, the modeling of more complex RVE architectures and the multiscale analysis are of interest. Further investigations are necessary regarding the role of the RVE depth on the stress distributions. The

authors are currently implementing a multiscale framework to verify the effects of the RVE modeling on the failure of a specimen with comparisons with experimental results.

Acknowledgements

This work is supported by the project ICONIC (Improving the Crashworthiness of Composite Transportation Structures), funded by the European Union Horizon 2020 Research and Innovation program under the Marie Skłodowska-Curie Grant agreement No. 721256.

References

[1] E.J. Barbero. *Multifunctional Composites*. Number v. 1 in Multifunctional Composites Series. CreateSpace Independent Publishing Platform, 2015.

[2] R. Talreja and C.V. Singh. *Damage and Failure of Composite Materials*. Cambridge University Press, 2012.

[3] J. Aboudi, S.M. Arnold, and B.A. Bednarcyk. *Micromechanics of Composite Materials: A Generalized Multiscale Analysis Approach*. Elsevier Science, 2013.

[4] D. Gay. *Composite Materials: Design and Applications, Third Edition*. CRC Press, 2014.

[5] R. Talreja and J. Varna. *Modeling Damage, Fatigue and Failure of Composite Materials*. Woodhead Publishing Series in Composites Science and Engineering. Elsevier Science, 2015.

[6] E.K. Gamstedt and B.A. Sjögren. Micromechanisms in tension-compression fatigue of composite laminates containing transverse plies. *Composites Science and Technology*, 59(2):167–178, 1999.

[7] M. Hinton, P.D. Soden, and A.S. Kaddour. *Failure Criteria in Fibre Reinforced Polymer Composites: The World-Wide Failure Exercise*. Elsevier Science, 2004.

[8] M. Mehdikhani, L. Gorbatikh, I. Verpoest, and S. V. Lomov. Voids in fiber-reinforced polymer composites: A review on their formation, characteristics, and effects on mechanical performance. *Journal of Composite Materials*, 53(12):1579–1669, 2019.

[9] C.T. Sun and R.S. Vaidya. Prediction of composite properties from a representative volume element. *Composites Science and Technology*, 56:171–179, 02 1996.

[10] S. Li and E. Sitnikova. *Representative Volume Elements and Unit Cells: Concepts, Theory, Applications and Implementation*. Woodhead Publishing Series in Composites Science and Engineering. Elsevier Science, 2019.

[11] C. Gonzalez and J. Llorca. Mechanical behavior of unidirectional fiber-reinforced polymers under transverse compression: Microscopic mechanisms and modeling. *Composites Science and Technology*, 67:2795–2806, 10 2007.

[12] J. Chevalier, P. Camanho, F. Lani, and T. Pardoen. Multi-scale characterization and modelling of the transverse compression response of unidirectional carbon fiber reinforced epoxy. *Composite Structures*, 209, 10 2018.

[13] T. Hobbiebrunken, M. Hojo, B. Fiedler, M. Tanaka, O. Shojiro, and S. Karl. Thermomechanical analysis of micromechanical formation of residual stresses and initial matrix failure in CFRP. *JSME International Journal Series A*, 47, 07 2004.

[14] L. Yang, X. Liu, Z. Wu, and R. Wang. Effects of triangle-shape fiber on the transverse mechanical properties of unidirectional carbon fiber reinforced plastics. *Composite Structures*, 152, 05 2016.

[15] F. Naya, C. González, C.s Lopes, S. Veen, and F. Pons. Computational micromechanics of the transverse and shear behavior of unidirectional fiber reinforced polymers including environmental effects. *Composites Part A: Applied Science and Manufacturing*, 92, 06 2016.

[16] V.P. Nguyen, O. Lloberas-Valls, M. Stroeven, and L. Sluys. Homogenization-based multiscale crack modelling: From micro-diffusive damage to macro-cracks. *Computer Methods in Applied Mechanics and Engineering*, 200:1220–1236, 02 2011.

[17] E.J. Barbero. *Finite Element Analysis of Composite Materials using AbaqusTM*. Composite Materials. Taylor & Francis, 2013.

[18] D. Garoz Gómez, F.A. Gilabert Villegas, R. Sevenois, S. Spronk, and W. Van Paepegem. Material parameter identification of the elementary ply damage mesomodel using virtual micro-mechanical tests of a carbon fiber epoxy system. *Composite Structures*, 181:391–404, 2017.

[19] A. Hyde, L. Liu, X. Cui, and J. Lua. Micromechanics-enriched finite element modeling of composite structures with fiber waviness and void defects. AIAA SciTech Forum, 01 2019.

[20] C.C. Chamis, F. Abdi, M. Garg, L. Minnetyan, H. Baid, D. Huang, J. Housner, and F. Talagani. Micromechanics-based progressive failure analysis prediction for WWFE-III composite coupon test cases. *Journal of Composite Materials*, 47(20-21):2695–2712, 2013.

[21] R. Talreja. *Incorporating manufacturing defects in damage and failure analysis*, pages 377–390. 12 2016.

[22] H. Jiang, Y. Ren, Z. Liu, and S. Zhang. Microscale finite element analysis for predicting effects of air voids on mechanical properties of single fiber bundle in composites. *Journal of Materials Science*, 54, January 2019.

[23] K. Chowdhury, R. Talreja, and A. Benzerga. Effects of manufacturing-induced voids on local failure in polymer-based composites. *Journal of Engineering Materials and Technology*, 130, 04 2008.

[24] J. Aboudi. The response of a partially loaded composite half-space weakened by local defects. *International Journal of Solids and Structures*, 168, 03 2019.

[25] M. Naderi and N. Iyyer. Micromechanical analysis of damage mechanisms under tension of 0-90 thin-ply composite laminates. *Composite Structures*, 234:111–659, 11 2019.

[26] A. Benzerga, X. Poulain, K. Chowdhury, and R. Talreja. Computational methodology for modeling fracture in fiber-reinforced polymer composites. *Journal of Aerospace Engineering*, 22, 07 2009.

[27] H. Huang and R. Talreja. Effects of void geometry on elastic properties of unidirectional fiber reinforced composites. *Composites Science and Technology*, 65:1964–1981, 10 2005.

[28] L. Zhuang and R. Talreja. Effects of voids on postbuckling delamination growth in unidirectional composites. *International Journal of Solids and Structures*, 51:936–944, 03 2014.

[29] D. Vajari, C. Gonzalez, J. Llorca, and B. Legarth. A numerical study of the influence of microvoids in the transverse mechanical response of unidirectional composites. *Composites Science and Technology*, 97, 06 2014.

[30] T. Huang and Y. Gong. A multiscale analysis for predicting the elastic properties of 3D woven composites containing void defects. *Composite Structures*, 185, 11 2017.

[31] I. Kaleel, M. Petrolo, A. Waas, and E. Carrera. Computationally efficient, high-fidelity micromechanics framework using refined 1D models. *Composite Structures*, 181, 08 2017.

[32] I. Kaleel, M. Petrolo, E. Carrera, and A. Waas. Micromechanical progressive failure analysis of fiber-reinforced composite using refined beam models. 11 2017.

[33] I. Kaleel, M. Petrolo, E. Carrera, Pineda. E.J., T.M. Ricks, B.A. Bednarcyk, and S.M. Arnold. Integration of CUF micromechanics framework into NASMAT for multiscale analysis of fiber-reinforced

composites. In ICMAMS, editor, *Proceedings of the Second International Conference on Mechanics of Advanced Materials and Structures - ICMAMS 2019, Nanjing, China*.

[34] E. Carrera, M. Cinefra, E. Zappino, and M. Petrolo. *Finite Element Analysis of Structures Through Unified Formulation*. John Wiley & Sons Ltd, 2014.

[35] I Kaleel, M Petrolo, E Carrera, and AM Waas. Computationally efficient concurrent multiscale framework for the linear analysis of composite structures. *AIAA Journal*, 57(9):4019–4028, 2019.

[36] I Kaleel, M Petrolo, E Carrera, and AM Waas. Computationally efficient concurrent multiscale framework for the nonlinear analysis of composite structures. *AIAA Journal*, 57(9):4029–4041, 2019.

[37] E. Carrera and M. Petrolo. Refined beam elements with only displacement variables and plate/shell capabilities. *Meccanica*, 47(3):537–556, 2012.

[38] R. Sevenois, G.D. Garoz, E. Verboven, S. Spronk, F. Gilabert, M. Kersemans, L. Pyl, and W. Van Paepegem. Multiscale approach for identification of transverse isotropic carbon fibre properties and prediction of woven elastic properties using ultrasonic identification. *Composites Science and Technology*, 168, 09 2018.

[39] D.C. Montgomery. *Applied Statistics and Probability for Engineers, 6th Edition*. John Wiley and Sons, Incorporated, 2013.

[40] J.M. Chambers. *Graphical Methods for Data Analysis*. CRC Press, 2018.